https://doi.org/10.5194/egusphere-2023-3047
Preprint. Discussion started: 20 December 2023

A survey of methane point source emissions from coal mines in Shanxi province of China using AHSI on board Gaofen-5B

Zhonghua He[1], Ling Gao[2], Miao Liang[3], Zhao-Cheng Zeng[4,*]

[1]Zhejiang Climate Centre, Zhejiang Meteorological Bureau, Hangzhou, 310052, China
[2]National Satellite Meteorological Centre, China Meteorological Administration, Beijing 100081, China
[3]Meteorological Observation Centre, China Meteorological Administration, Beijing, 100081, China
[4] Institute of Remote Sensing and GIS, School of Earth and Space Sciences, Peking University, Beijing, 100871, China

Correspondence to: Z.-C. Zeng (zczeng@pku.edu.cn)

Abstract. Satellite-based detection of methane (CH_4) point sources is crucial in identifying and mitigating anthropogenic emissions of CH_4, a potent greenhouse gas. Previous studies have indicated the presence of CH_4 point source emissions from coal mines in Shanxi, China, an important source region with large CH_4 emissions, but a comprehensive survey has remained elusive. This study aims to conduct a survey of CH_4 point sources over Shanxi's coal mines based on observations of the Advanced HyperSpectral Imager (AHSI) on board the Gaofen-5B satellite (GF-5B/AHSI) between 2021 and 2023. The spectral shift in center wavelength and change in full-width-half-maximum (FWHM) are estimated for all spectra channels, which are used as inputs for retrieving the enhancement of column-averaged dry-air mole fraction of CH_4 (ΔXCH_4) using a matched-filter based algorithm. Our results show that the spectral calibration on GF-5B/AHSI reduced estimation biases of emission flux rate by up to 5.0%. We applied the flood-fill algorithm to automatically extract emission plumes from ΔXCH_4 maps. We adopted the integrated mass enhancement (IME) model to estimate the emission flux rate values from each CH_4 point source. Consequently, we detected CH_4 point sources in 32 coal mines with 93 plume events in Shanxi province. The estimated emission flux rate ranges from 857.67 ± 207.34 kg·h^{-1} to 14333.02 ± 5249.32 kg·h^{-1}. The total emission flux rate reaches 13.26 t·h^{-1} in Shanxi, assuming all point sources emit simultaneously. Our results show that wind speed is the dominant source of uncertainty contributing about 84.84% to the total uncertainty in emission flux rate estimation. Interestingly, we found a number of false positive detections due to solar panels that are widely spread in Shanxi. This study also evaluates the accuracy of wind fields in ECMWF ERA5 reanalysis by comparing with ground-based meteorological station. We found large discrepancy, especially in wind direction, suggesting incorporating local meteorological measurements into the study CH_4 point source are important to achieve high accuracy. The study demonstrates that GF-5B/AHSI possesses capabilities for monitoring large CH_4 point sources over complex surface characteristics in Shanxi.

1 Introduction

Due to its potent radiative forcing and relatively short lifespan of about a decade, methane (CH_4), the second most significant anthropogenic greenhouse gas after atmospheric carbon dioxide, is an effective target that attracts increasing attention for emission reduction and climate change mitigation (**IPCC, 2021**). Human activity related sources of atmospheric CH_4 primarily include agricultural activities like livestock farming and rice cultivation, industrial processes such as petroleum, natural gas, and coal extraction, as well as landfills and waste management (**Lu et al., 2022**). Among these, industrial activities related to fossil fuel production contribute to nearly 35% of global anthropogenic CH_4 emissions (**Saunois et al., 2020**), not only triggering the greenhouse effect but also leading to significant energy wastage (**Chen et al., 2023**). Methane emissions escaping from energy production activities primarily stem from industrial infrastructure emissions, such as wells, collection and compression stations, storage tanks, pipelines, and processing plants, easily forming "point sources" of CH_4 emissions (**Varon et al., 2019**). With the destruction of geological processes involved in mining activities, the release of coalbed methane captured in coal seams and surrounding rock strata forms the point source of CH_4 emission from coal mines (**Zheng et al., 2019**). These emissions plumes of gas release from point sources contain high concentrations of CH_4 over relatively small surface areas (**Duren et al., 2019**). The overall plumes formed by point source emissions exhibit a notable heavy-tailed distribution (**Irakulis-Loitxate et al., 2021**). However, due to the comprehensive effect of emission magnitude, land cover types, wind speed and direction, these plumes often show different characteristics across different time and space changes (**Sánchez-García et al., 2022**), which makes the plume detection and emission estimation challenging. Given that such emissions contribute significantly to regional CH_4 emissions (**Frankenberg et al., 2016**), it is important to have accurate detection and estimation. As atmospheric CH_4 is colourless and odourless, coupled with the strong uncertainty in the temporal and spatial distribution of point source emissions, satellite remote sensing using high resolution spectroscopy has become a crucial means for detecting CH_4 point source emissions due to its high sensitivity, wide coverage and high revisit capabilities (**Pandey et al., 2021**).

Satellite observations for detecting global atmospheric CH_4 concentrations with high spatiotemporal resolution, provides data support for accounting and assessing reduction measures (**Jacob et al., 2022**). Satellite detection and quantification of CH_4 super-emitters was first demonstrated in the 2015 Aliso Canyon blowout incident using the Hyperion imaging spectrometer on board EOS-1 (**Thompson et al., 2016**). Satellites with high spatial resolution but with moderate spectral resolution have successfully detected and traced CH_4 point source emissions. The currently in orbit satellites include Canada's GHGSat (2016-present; **Jervis et al., 2021**), Italy's PRISMA (2019-present; **Guanter et al., 2021**), China's GF-5 and ZY-1 satellites (**Irakulis-Loitxate et al., 2021**), NASA's EMIT (**Thorpe et al., 2023**), and the German EnMAP mission (**Guanter et al., 2015**). While multispectral (Landsat-8/9, Sentinel-2, and WorldView-3) and coarse-resolution high-spectral satellites (Sentinel-5P TROPOMI) have also been widely validated for detecting extra-large CH_4 plumes (**Ehret et al., 2022**; **Varon et al., 2021**; **Sanchez-Garcia et al., 2022**; **Lauvaux et al., 2022**), limitations in spectral or spatial resolution result in differences in detection sensitivity, estimation uncertainty, and tracing capabilities. The first generation AHSI on board China's GF-5A (GF-

https://doi.org/10.5194/egusphere-2023-3047
Preprint. Discussion started: 20 December 2023

5A/AHSI) exhibits high capabilities in detecting CH_4 point source emissions. As shown in **Irakulis-Loitxate et al. (2021)**, 37 unexpected emission point sources exceeding 500 kg·h^{-1} can be identified in the Permian Basin oil and gas fields using images from GF-5A and PRISMA satellites, illustrating the potential of AHSI in regional CH_4 point source survey. To estimate emissions from CH_4 point source, these studies typically employ spectral matching filtering method to derive CH_4 increment ($\triangle XCH_4$) and then estimate flux rate using integrated mass enhancement (IME) model (**Varon et al., 2018**). These studies have previously provided available techniques in the identification of point sources in local or national scales (e.g., Algeria, Permian, China, USA), and flux estimation and uncertainty analyses for these point sources (**Guanter et al., 2021; Irakulis-Loitxate et al., 2021**).

As the world's largest coal producer, China contributes 50.7% of the global coal production in 2020, making it one of the largest emitters of CH_4 from coal mining (**Chen et al., 2022b**), especially in Shanxi province, where most underground coal mines are located **(Qin et al., 2023)**. However, due to the influence of complex surface conditions on the background spectral characteristics, satellite observations exhibit notably lower sensitivity in the detection of CH_4 point source emissions in Shanxi compared to other regions with more homogeneous land surfaces (**Sánchez-García et al., 2022; Guanter et al., 2021**). In addition, the wind fields from reanalysis datasets may be subject to high uncertainty due to the complex terrain in Shanxi, making the detection of plumes challenging and leading to highly uncertain emission flux rate estimation (**Jongaramrungruang et al., 2021**). Although TROPOMI imagery and convolutional neural networks haven been shown to effectively detect potential large CH_4 emission point sources globally (**Schuit et al., 2023**), the specific localization and tracing of CH_4 emission point sources in China remain difficult due to the limitations of coarse spatial resolution and complex regional backgrounds, warranting further surveying efforts.

This study aims to conduct a survey of the CH_4 point source plumes in Shanxi by developing a framework to detect and estimate emissions flux rate using the latest hyperspectral observations from GF-5B/AHSI from 2021 to 2023. Specifically, this study focuses on (1) quantifying the impact of the shift in spectral wavelength and the change in spectral instrument line shape (ILS) for the spectral channels of GF-5/AHSI on CH_4 retrieval and emission estimation; (2) Identifying CH_4 point source plumes using the matched filter method; (3) automating the segmentation of emission plumes from the retrieved CH_4 enhancement maps; (4) Estimating emissions flux rate from point sources using IME method; (5) Understanding the spatial and temporal patterns of CH_4 emissions from point sources in Shanxi.

2 Study area and used datasets

2.1 Study area

Shanxi Province is the most extensively mined region in China, harbouring nearly half of the nation's suspected point sources based on TROPOMI observations (**Schuit et al., 2023**). It stands as a typical area for CH_4 point source emissions in China and has been a focal point in prior comparative studies on point source emissions (**Sanchez-Garcia et al., 2022; Guanter et al.,**

2021). Shanxi Province (**Figure 1**), situated in northern China, experiences a temperate continental monsoon climate characterized by cold, dry winters and hot, humid summers. The region boasts diverse topography, comprising mountains, plateaus, and basins. Consequently, the stable atmospheric conditions during winter can lead to the accumulation of pollutants closer to the ground, impacting the detection of CH_4 emissions. Although the region has strict rules in regulating the process of CH_4, a by-product of coal mining, underground coal mines in Shanxi releases CH_4 from ground may come from abandoned coal mines or illegal mining (**Chen et al., 2022a**). Therefore, the identification of these plumes will help mitigate CH_4 emissions over this region.

2.2 GF-5B/AHSI dataset

The GF-5B satellite is the 2nd satellite of the Gaofen-5 series and was launched on September 7, 2021. It has accumulated over two years' worth of global observational data to date. Equipped with the Advanced Hyperspectral Imager (AHSI), it can capture spectral information spanning 400 to 2500 nm with a spatial resolution of 30 meters over a 60 km swath, encompassing 330 spectral channels with spectral resolutions of 5 and 10 nm in the VNIR and SWIR, respectively (**Liu et al., 2019**). Its relatively high signal-to-noise ratio (around 500 in the Short-Wave Infrared, SWIR) presents notable advantages in detecting CH_4 point source emissions (**Irakulis-Loitxate et al., 2021**). The retrieval of the enhancement of column-averaged dry-air mole fraction of CH_4 (ΔXCH_4) relies primarily on strong CH_4 absorption features near 2300 nm, while the 2100 to 2450 nm spectral window of the GF-5B/AHSI demonstrates higher sensitivity to XCH_4 variations, thereby possessing enhanced capabilities for precise CH_4 concentration inversion. This study focuses on Shanxi Province, using images from 111 GF-5B/AHSI scenes covering suspected point sources from September 2021 to September 2023, with a cloud cover of less than 10%, employed for ΔXCH_4 inversion and point source identification (**Figure 1b**). These images cover the major emission hotspots as identified by TROPOMI data (**Schuit et al., 2023**). Noted that, in Shanxi, the overpassing time of GF-5/AHSI is around 11-12 Beijing Time (BJT).

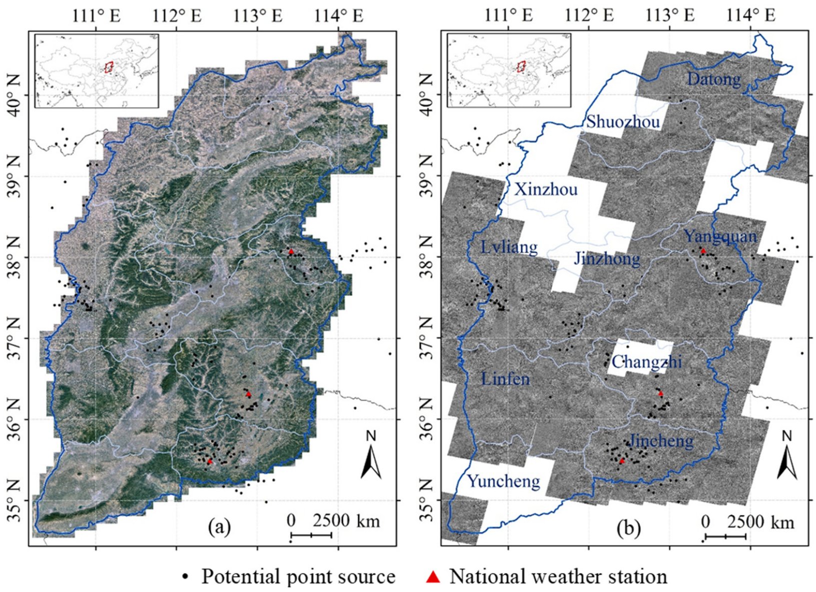

Figure 1. (a) The study area in Shanxi enclosed by the blue boundary, and (b) Gaofen-5B observed scene images used for the CH_4 plume survey. The black dots represent the potential point sources detected by TROPOMI (Schuit et al., 2023). The red dots represent the three national weather stations for monitoring meteorological variables in Yangquan, Changzhi, and Jincheng used for wind fields comparison with ERA5 reanalysis (Section 4.3).

2.3 Auxiliary data

Methane point source detection and emission estimation involve various auxiliary datasets, mainly including: (1) Ultra-high-resolution surface imagery for checking false positive in point source detection; (2) Wind fields information for estimate emissions from point source plumes; (3) Digital Elevation Model (DEM) data for the geometric correction of AHSI imagery. High-resolution surface imagery is an indispensable dataset in point source identification and serves as direct evidence for distinguishing interference signals. The high-resolution imagery used in this study primarily comes from Google Earth. Wind speed data is a critical parameter for calculating emission flux rates. The study utilized U_{10} hourly wind speed reanalysis products from ECMWF ERA5, with a spatial resolution of 0.25x0.25 degrees (**Muñoz-Sabater et al., 2021**). Terrain data is crucial for the geometric correction of AHSI imagery, directly impacting the positioning and identification of ΔXCH_4 plume signals. The study used DEM data from STRM (**Farr et al., 2007**), with a spatial resolution of 30 meters. Additionally, the study obtained hourly meteorology monitoring data, including wind speed and wind direction, from January 2021 to September 2023 from three national meteorological stations in Yangquan, Changzhi, and Jincheng (**Figure 1**), obtained from the China

Meteorological Administration Data Centre. These data were compared with ERA5's U_{10} hourly wind speed reanalysis products to investigate the uncertainty of the ERA5's wind field.

3 Methods

The retrieval of ΔXCH_4 and estimation of emission flux rate from high-resolution hyperspectral data have been implemented in many previous studies (e.g., **Cusworth et al., 2020; Guanter et al., 2021; Huang et al., 2020; Varon et al., 2018; Frankenberg et al., 2016**) using matched filter method and the IME model, respectively. This study primarily applies these two methods to survey the CH_4 point source emissions in Shanxi using GF-5B/AHSI. In addition, this study focuses on the quantification the impact of the spectral shift and the change in spectral ILS on the point source emission estimation, the automation of the segmentation of emission plumes from the retrieved CH_4 enhancement maps, and the analysis of the spatial and temporal patterns of CH_4 emissions from point sources in Shanxi.

3.1 ΔXCH_4 retrieval using matched filter method

3.1.1 Spectral calibration of GF-5B/AHSI

Spectral shift of centre wavelength and change in FWHM relative to the nominal spectral calibration for spectral channels significantly affects the retrieval results of ΔXCH_4 using spectral matched filter method (e.g., **Guanter et al., 2021**). The spectral shift and FWHM change vary distinctly between different image scenes. It is therefore important to re-calibrate the spectra for all channels before further analysis using the observed spectra. While GF-5B AHSI imagery has been utilized in CH_4 point source detection experiments in various regions, estimation regarding its spectral offset and associated correction in FWHM have not yet been undertaken. In this study, we conduct this spectral calibration for the Short-Wave Infrared (SWIR) channels from 2110 nm to 2455 nm of GF-5B/AHSI data (**Guanter et al., 2009**). The basic idea of the spectral calibration is to retrieve the wavelength shift and FWHM change that would lead to the best fit between observed GF-5B/AHSI spectra and the simulated spectra based on radiative transfer model. In practice, we used the forward radiative transfer model and optimal estimation method in GFIT3 (**Zeng et al., 2021**) to iteratively derive the spectral calibration parameters. Similar to **Guanter et al. (2021)**, we applied the calibration to the averaged top-of-the-atmosphere radiance from all observations of each across-track detector and derive the wavelength shift and FWHM change. This calibration is repeated for all detectors and over all GF-5B/AHSI images. Eventually, the updated spectral centre wavelength and FWHM for all channels are used as inputs in the ΔXCH_4 retrieval when the high-resolution CH_4 absorption spectra is convolved with Gaussian ILS.

3.1.2 Spectral matched filter for retrieving ΔXCH_4

Spectral matched filter method derives the ΔXCH_4 by calculating the difference between the “polluted” spectra over a source region with background spectra of the ambient atmosphere, and expressing the difference by the number of target absorption spectrum from one unit of XCH_4 (e.g., 1 ppm of XCH_4; **Guanter et al., 2021**). The retrieval using matched filter is depicted in **Equation (1)**:

$$\Delta XCH_4 = ((\boldsymbol{x} - \boldsymbol{\mu})^T \Sigma^{-1} \boldsymbol{t}) / (\boldsymbol{t}^T \Sigma^{-1} \boldsymbol{t}) \quad (1)$$

Where, $\boldsymbol{x}$ denotes a vector of the observed SWIR hyperspectral spectra from a target pixel. In this study, the CH_4 strong absorption band (2110-2455 nm) is used; $\boldsymbol{\mu}$ and Σ represent the mean and covariance of the SWIR hyperspectral observation over background regions, respectively. $\boldsymbol{t}$ is target spectrum, representing the disturbance vector of SWIR hyperspectral due to enhanced XCH_4 relative to the background. It can be derived from an element-wise multiplication of $\boldsymbol{\mu}$ and the unit XCH_4 absorption spectrum $\boldsymbol{\kappa}$, which is generated from GFIT3 (**Zeng et al., 2021**), as shown in **Figure 2**, assuming a perturbation of 1 ppm XCH_4.

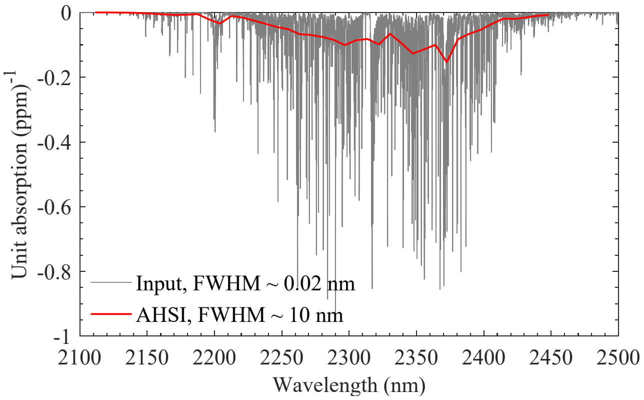

Figure 2. Example of unit XCH_4 absorption spectrum used as target signature in the matched filter retrieval method. The high-resolution target signature (in grey) represents absorptivity induced by 1 ppm XCH_4 enhancement, which is calculated using GFIT3 (Zeng et al., 2021). The high-resolution absorptions are then convolved with a Gaussian ILS with nominal FWHM from GF-5B/AHSI to derive the spectra (in red) that can be compared with observed from AHSI.

3.2 Identifying point source plumes from ΔXCH_4 maps

After data pre-processing, including spectral re-calibration and ΔXCH_4 retrieval, we implemented a geometric localization to change the GF-5B/AHSI imagery index for row and column pixels to latitude and longitude under WGS84 projection. The detailed description of this geometric localization is in the **Appendix A**. Then, this study compares the ΔXCH_4 maps with high-resolution Google Earth imagery to visually inspect and preliminarily identify the CH_4 point source plumes. The identification criteria include: (1) high ΔXCH_4 values displaying plume characteristics; (2) the presence of ground facilities such as factories or pipelines representing potential CH_4 emission sources; (3) plume distribution characteristics not caused by terrain features that may impact short-wave infrared strong absorption in surface features. Although wind conditions directly affect plume features, however, reanalysis data (e.g., ERA5) of wind direction may be very differ from the plume structure.

Therefore, this study temporarily refrains from utilizing wind direction from ERA5 reanalysis as a direct criterion for point source identification.

3.3 Estimation of emission flux rates

3.3.1 Automatic segmentation of ΔXCH_4 plumes using flood-fill algorithm

The segmentation of ΔXCH_4 plumes in previous studies have often been manually drawn, a laborious and time-consuming process highly influenced by subjective human judgment, leading to possible bias in IME calculations. Hence, there's a need to introduce a statistically-based, relatively objective, and easy to implement method for ΔXCH_4 plume segmentation. The flood-fill algorithm has been widely employed for segmenting and extracting continuous abnormal signals (**He et al., 2018; Zscheischler et al., 2013**), showing potential for ΔXCH_4 plume automatic segmentation. Specifically, this study uses statistical parameters, including ΔXCH_4 mean and one standard deviation, within the study area to segment and identify concentration-enhanced signals of ΔXCH_4. It employs the flood-fill algorithm to recognize abnormal pixels in the vicinity of eight directions, merging spatially connected pixels into a plume pattern by considering the spatial continuity of plumes.

3.3.2 Estimation of CH_4 point source emission flux rates

For emission flux rate estimation, this study employs the IME model (**Equation (2); Frankenberg et al., 2016; Varon et al., 2018; Guanter et al., 2021**) to calculate the excess mass of CH_4 in the plumes relative to the background from the retrieved ΔXCH_4 plume maps. Then the emission flux rate (Q) is calculated using **Equation (3)** with inputs of wind speed and the length of the plume. These equations are:

$$IME = k\sum_{i=1}^{n_p} \Delta \mathrm{XCH_4}(i) \tag{2}$$

$$Q = ((\alpha \cdot U_{10} + \beta) \cdot IME)/L \tag{3}$$

where n_p denotes the number of pixels in the plume; $\Delta \mathrm{XCH_4}(i)$ represents the XCH_4 enhancement in pixel i; k is the scaling factor (5.155×10^{-3} kg·ppb^{-1}), which is the same as **Guanter et al. (2021).** k converts ΔXCH_4 from volume mixing ratio to mass based on Avogadro's law, considering the pixel resolution of GF-5B/AHSI to be 30-meter; Q denotes the point source emission rate, in unit of mass per unit time, obtained from IME calculation; $(\alpha \cdot U_{10} + \beta)$ denotes the effective wind speed derived from wind speed at 10-meter from ERA5 reanalysis; L is the plume length, defined as the square root of the plume mask area (**Varon et al., 2018**). α and β can be determined through Large Eddy Simulation based on the spatial resolution of satellite observation and ΔXCH_4 retrieval accuracy from GF-5B/AHSI. In this study, we adopted the estimates (α=0.37 and β=0.64) from **Li et al. (2023)** derived for the Changzhi region in Shanxi. Globally, the values of α and β do not change significantly. For example, the values adopted for PRISMA (**Gaunter et al., 2021; Irakulis-Loitxate et al., 2021**) were 0.34 and 0.44, and for GF-5B in the Permian basin (**Li et al., 2023**) were 0.38 and 0.41, respectively.

https://doi.org/10.5194/egusphere-2023-3047
Preprint. Discussion started: 20 December 2023

3.3.3 Estimation uncertainty of point source emission flux rate

The uncertainty of point source emission flux rate typically involves two primary aspects: the IME calculation and wind speed. For the IME calculation based on the flood-fill plume extraction, (1) the background selection in the study area and (2) the threshold setting for plume enhancement segmentation are the main factors involved. Referring to the uncertainty assessment method by **Cusworth et al. (2020)**, we first assess the uncertainty of IME and then propagate the random errors of IME and wind speed (U_{10}) to the flux rate Q, thereby evaluating the uncertainty of the estimated emission flux rate. In practice, for IME calculation for a certain plume, we first define a background region in square (with length of 600 pixels, which is 18 km) and a threshold of 0.5σ for the flood-fill algorithm that can effectively segment the point source plume. The σ is one standard deviation of ΔXCH_4 values in the background region. For each iteration in the assessment of IME uncertainty, we adjusted the background square length with an interval of 2.4 km, from 12 km to 24 km (in total 6 iterations). Simultaneously, we adjusted the threshold for identification by 0.02σ from 0.45σ to 0.55σ (in total 6 iterations). This process enabled the extraction of 36 reasonable plume values, defining their standard deviation as the uncertainty of IME. For the wind speed uncertainty, to be consistent with the previous study, we set it at 50% for U_{10} (**Cusworth et al., 2020; Guanter et al., 2021**). To further understand the uncertainty of the used wind uncertainty, in Section 4.3, we have carried out an evaluations of wind speeds and wind directions from ERA5 reanalysis by comparison with observations from meteorological sites in Shanxi.

4 Results

4.1 Detection and estimation of emission flux rate for single CH_4 point source using GF-5B/AHSI

Figure 3 demonstrates the retrieval results of point sources ΔXCH_4 based on multiple capturing of the same point source using GF-5B/AHSI from January 2022 to August 2023. Under different emission flux rates and wind conditions, the emission plumes exhibited various characteristics. Six observations occurred during the winter-spring seasons (**Figure 3(b)-(g)**), showing ΔXCH_4 plumes spreading north-eastward, while the observation in summer (**Figure 3(h)**) displayed a plume drifting north-westward. This result indicates that emissions from the same point source observed at different times might significantly differ. An intriguing aspect is the occurrence of two repeated observations of the same point source within an 8-second interval (**Figure 3(d) and (e), Figure 3(f) and (g)**). Theoretically, CH_4 emissions from the same point source within an 8-second interval should exhibit very similar patterns. However, using the whole scene image as the background for each plume, similar to previous studies, the ΔXCH_4 of the plumes from the same point source showed large differences, especially for **Figure 3(f) and (g)**. The notable difference primarily arises from the different background used, suggesting the importance of selecting appropriate background regions. Noted that the difference may also be slightly caused by the different signal noise ratio, as the plumes appears at different locations of the imaging scene. The plumes appear at the bottom of the scene in **Figure (f)** and at the top in **Figure (g)**.

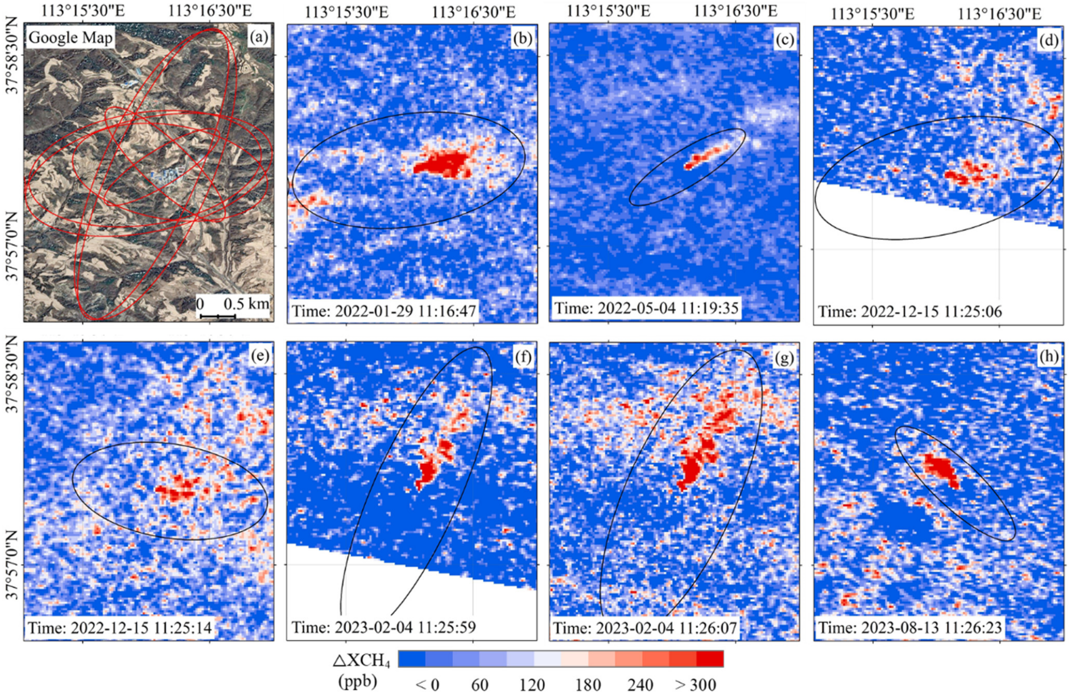

Figure 3. Example of ΔXCH_4 retrievals from one typical single point source with multiple overpasses by GF-5B/AHSI. (a) shows the background image from © Google Maps with ellipse shapes (in red and black) indicating the elongated directions of detected plumes from the seven events detected in (b)-(h). The observation time in Beijing Time is shown for each plume event.

Based on the ΔXCH_4 retrieval and the flood-fill plume segmentation method, we obtained the plume characteristics and emission flux rate of the seven detections, as shown in **Figure 4**. The results indicate the following: (1) differences exist between the extracted plume features and visual segmentation. For instance, in **Figure 4(c)**, the elaborate plume automatically extracted using flood-fill would be challenged for manually drawing; (2) the point source emission flux rate varies between 3195.66 ± 1495.03 $kg \cdot h^{-1}$ in **Figure 4(e)** and 7520.26 ± 2606.74 $kg \cdot h^{-1}$ in **Figure 4(g)** (excluding incomplete observations in **Figure 4(d)**). Among these observations, four fall within a similar range between 3195 and 3661 $kg \cdot h^{-1}$; (3) the uncertainty of IME ranges from 5.07% to 66.38%, with the majority being below 30%, which is lower than the uncertainty caused by wind speed (~50%) in the emission flux rate calculation; (4) significant differences are evident in the plumes from adjacent detections of the same point source (e.g., **Figure 4(f) and (g)**), indicating the different backgrounds chosen for different imagery scenes are not optimal to monitoring the same emission plumes.

https://doi.org/10.5194/egusphere-2023-3047
Preprint. Discussion started: 20 December 2023

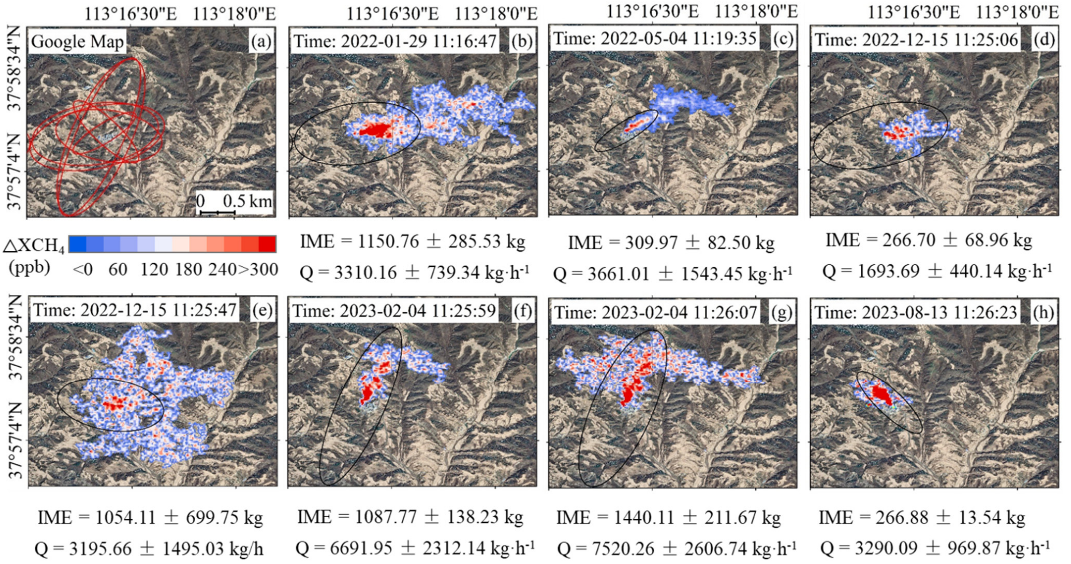

Figure 4. Examples of extracted CH_4 point source plume using flood-fill method based on the retrieved ΔXCH_4 maps, as shown in Figure 3, from a single point source with multiple overpasses by GF-5B/AHSI. The ellipse shapes (in red and black) indicating the elongated directions of detected plumes from the seven events. The plume mass from IME model and the estimated emission flux rates are also indicated at the bottom of each map. The observation time in Beijing Time is shown for each plume event. All background images ((a) – (h)) are from © Google Maps.

In order to eliminate the impact of background selection on estimating emission flux rate from the same point source, this study conducted a ΔXCH_4 retrieval experiment using overlapping area in the imagery maps of **Figure 3(f)** and **(g)** as the new background. The results based on the new backgrounds shown in **Figure 5** demonstrate highly similar ΔXCH_4 plume features between the two observations that are 8 seconds apart (**Figure 5(a)** and **(b)**). The extracted plume distribution and emission flux rate calculations shown in **Figure 5(c)** and **(d)** are almost identical. The integrated enhanced masses were 1126.80 ± 15.74 kg and 1178.08 ± 17.15 kg, respectively, with emission flux rates of 6176.07 ± 2072.35 kg·h^{-1} and 6457.54 ± 2166.80 kg·h^{-1}. This reduced estimation discrepancy between the two by 546.84 kg·h^{-1} which is about 8.5% of the emission flux rate.

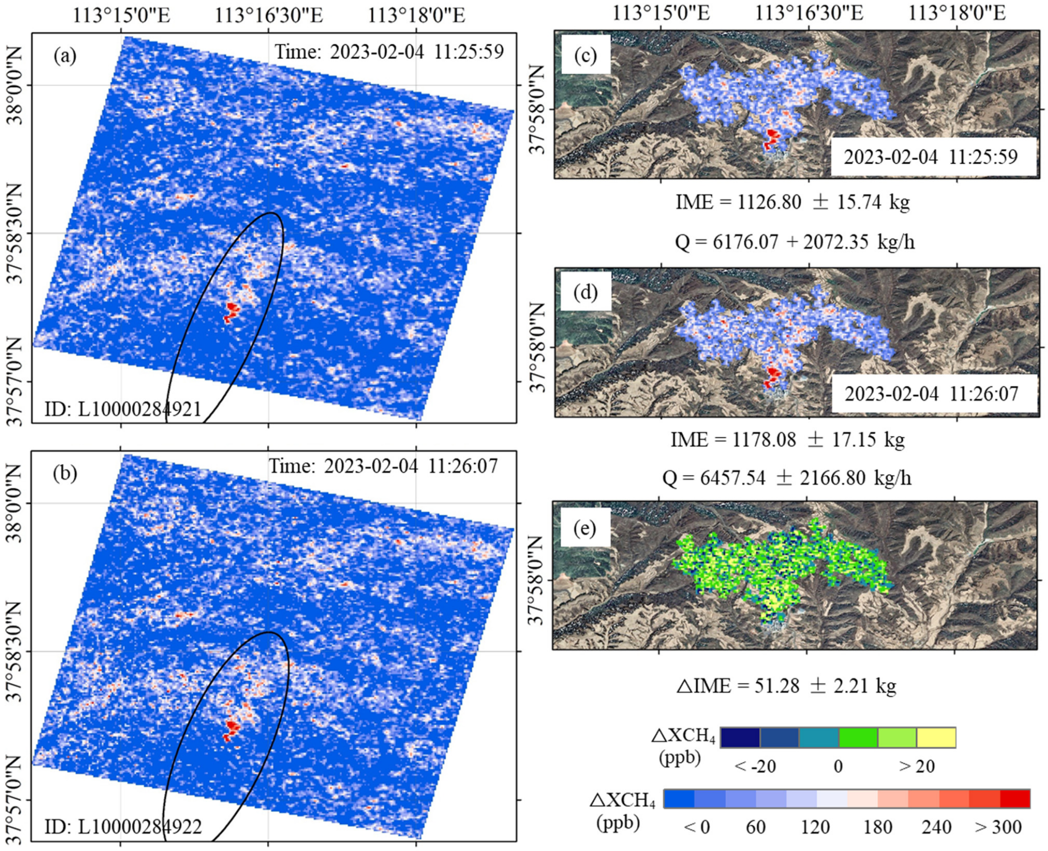

275 **Figure 5. ΔXCH_4 retrievals from GF-5B/AHSI observations that are 8 seconds apart in (a) and (b) over the same point source. The retrievals are carried out using the same background region. The ellipse shapes (in black) indicate the elongated directions of detected plumes from the plume event; The corresponding IME values and emission flux rates (Q) based on the extracted ΔXCH_4 maps are shown in (c) and (d), respectively. The difference of the two IME values is shown in (e). All background images ((c) – (e)) are from © Google Maps.**

4.2 Spatial distribution of point sources and their emission rates in Shanxi

280 Based on the methods described above for estimating CH_4 emission flux rate of point sources, we conducted a survey of all detectable point source emissions using all available imagery of GF-5B/AHSI from 2021 to 2023. In total, 93 point source plumes were identified. After averaging repetitive observations over the same point sources, a total of 32 point sources were identified, and their spatial distribution is depicted in **Figure 6. Figures 6(a)-(i)** exhibit typical plume extraction results around

https://doi.org/10.5194/egusphere-2023-3047
Preprint. Discussion started: 20 December 2023

three typical cities of Yangquan, Changzhi, and Jincheng. The emission flux rates range from 2421.80 ± 481.12 to 10360.80 ± 2313.59 kg·h^{-1}. This result demonstrates a reasonably good consistency between the spatial locations of the actual CH_4 emission point sources identified in this study (red dots in **Figure 6**) and those extracted based on TROPOMI data (black dots in **Figure 6**), primarily concentrated around the three cities of Yangquan, Changzhi, and Jincheng. Given its high spatial resolution, the spatial locations derived from GF-5B/AHSI are expected to be more accurate. We found that the number of identified point sources is much fewer than those extracted from TROPOMI. This is primarily attributed to the much denser observations from TROPOMI with daily global coverage. In addition, the high-resolution of the ΔXCH_4 retrieval results helped eliminate false positive signals due to surface interference elements like photovoltaic panels and greenhouse cultivation structures that are ubiquitous in Shanxi. Driven by wind speed and topography, different plumes from various point sources show distinctly varying dispersion distances, ranging from less than 1.0 km (e.g., **Figure 6(h)**) to 5.0 km (e.g., **Figure 6(d)**). Given that ΔXCH_4 retrieval is significantly influenced by the selection of background spectra, information of the length of the plumes is crucial in monitoring the emission flux rate.

We further conducted IME calculations and emission flux rate estimations for the 93 plumes extracted from GF-5B/AHSI (**Figure 7(a)** and **(c)**). Additionally, based on multiple observations (from 2 to 8 times) of the same point source, we provided the highest and lowest emission flux rates and IME for the same point source (**Figure 7(b) and (d)**). The survey results revealed a diverse range of point source emission flux rates, varying from 857.67 ± 207.34 (minimum) to 14333.02 ± 5249.32 kg·h^{-1} (maximum), with an average of approximately 4562.48 kg·h^{-1}. The IME of point source emissions ranges from 37.79 ± 7.04 (minimum) to 7423.09 ± 2169.19 kg (maximum), showcasing an inconsistent distribution between IME and emission flux rates due to the influence of wind conditions. Moreover, assuming a 50% uncertainty in U_{10} (wind speed at 10-meter), in the calculation uncertainty of Q (emission flux rate), the impact of wind speed and IME uncertainties accounts for approximately 84.84% and 15.16%, respectively. This implies that wind speed remains the dominant factor contributing to the uncertainty in estimating CH_4 point source emissions. However, the uncertainty related to IME remains important and cannot be overlooked. Furthermore, multiple observations of the same point source indicate significant variations in CH_4 emissions over time. The difference is as large as 11497.79 kg·h^{-1}, which is about 7 times between the maximum and the minimum, as shown in **Figure 7(d)**. This difference suggests that single observation does not adequately represent the overall or averaged emission scenario for any point source. To evaluate the total emissions from all point sources detected in the study area, we used the median of multiple observations for each point source to represent its emission rate. Assuming simultaneous emissions from all sources, the overall emission flux rate in Shanxi reaches 13.26 t·h^{-1}. This represents a considerable amount of CH_4 emissions that might significantly contribute to the total anthropogenic greenhouse gas emissions in China.

https://doi.org/10.5194/egusphere-2023-3047
Preprint. Discussion started: 20 December 2023

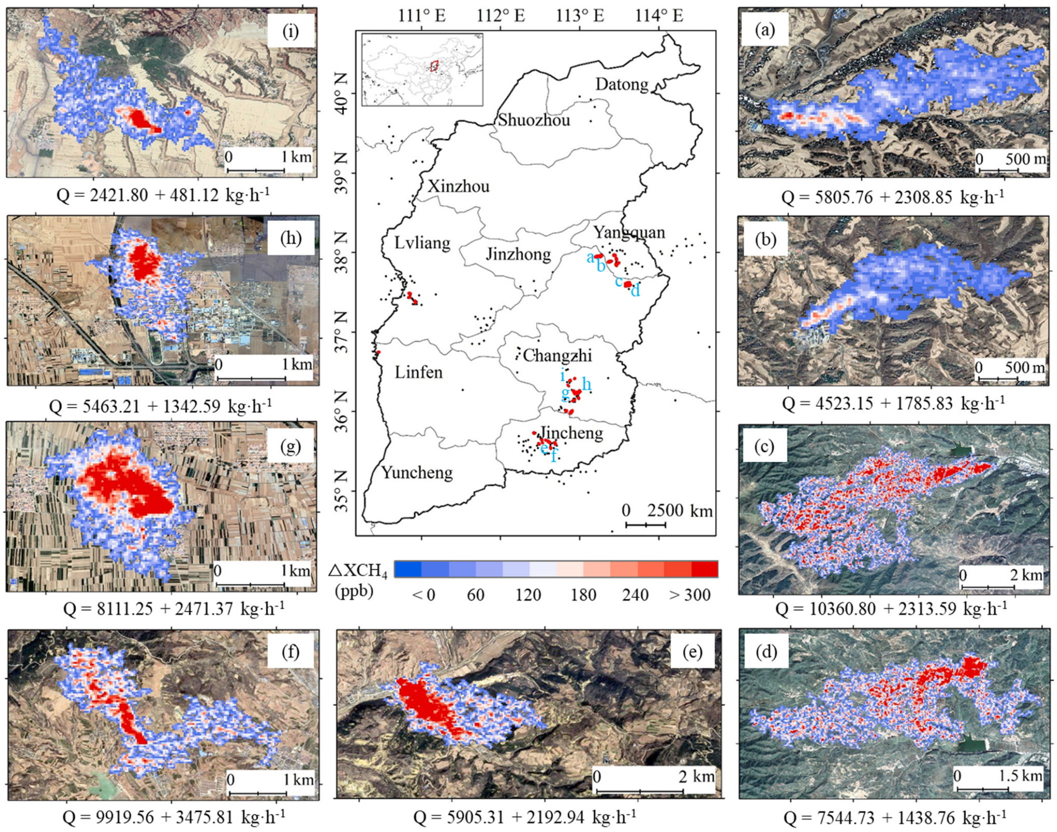

Q = 2421.80 + 481.12 kg·h^{-1}

Q = 5463.21 + 1342.59 kg·h^{-1}

Q = 8111.25 + 2471.37 kg·h^{-1}

Q = 9919.56 + 3475.81 kg·h^{-1}

Q = 5905.31 + 2192.94 kg·h^{-1}

Q = 5805.76 + 2308.85 kg·h^{-1}

Q = 4523.15 + 1785.83 kg·h^{-1}

Q = 10360.80 + 2313.59 kg·h^{-1}

Q = 7544.73 + 1438.76 kg·h^{-1}

Figure 6. The spatial distribution of the identified CH_4 plumes (in red dots; in total of 93) in Shanxi using GF-5B/AHSI observations, as shown in the centre panel. The black dots represent the potential point sources detected by TROPOMI (Schuit et al., 2023). CH_4 plumes (a)-(i) are examples of the identified ΔXCH_4 plumes in Shanxi. All background images ((a) – (i)) are from © Google Maps.

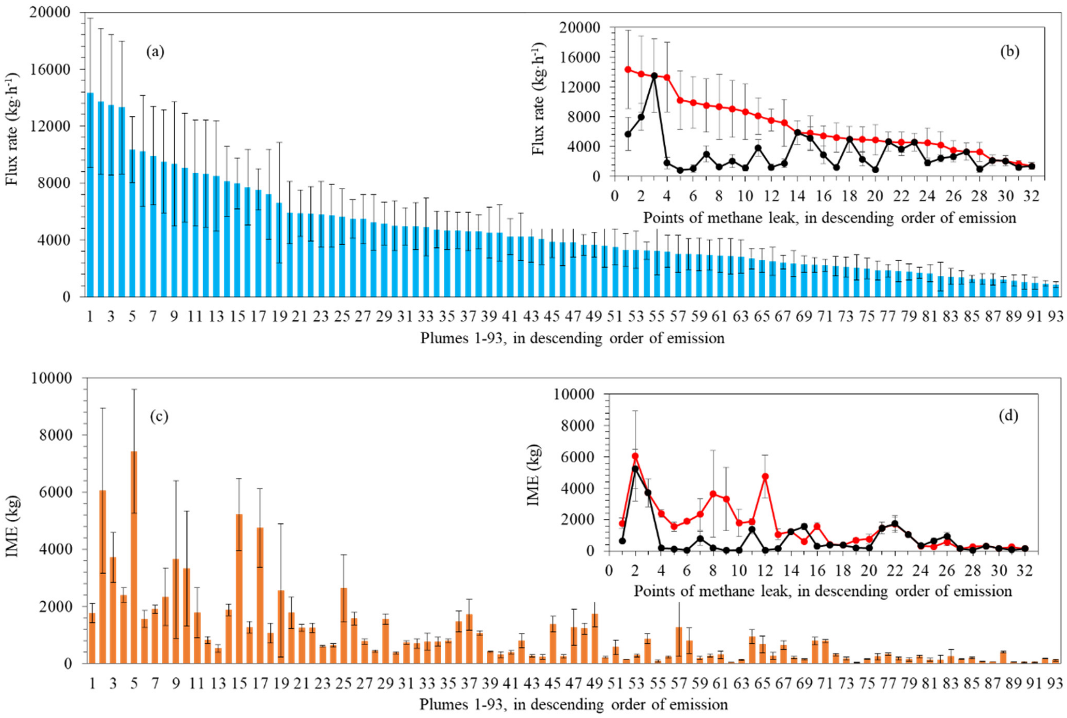

Figure 7. (a) CH_4 emission flux rate from point source plumes #1-#93 in descending order of emissions, with the error bars representing the estimation uncertainty; (b) The maximum and minimum emission flux rates for each point source with more than 2 observations; (c) The corresponding IME estimates for plumes #1-#93 following the order in (a); (d) The maximum of minimum emission flux rates for each point source with more than 2 observations.

4.3 Improvements on ΔXCH_4 retrieval and emission flux rate estimation

(1) Spectral calibration of GF-5B/AHSI observations

The impact of the wavelength shift and changes in FWHM of the spectral observations from GF-5B/AHSI on deriving ΔXCH_4 is demonstrated in **Figures 8 and 9**. **Figure 8** illustrates an example of the cross-track pixel variations of the estimated centre wavelength in (a) and FWHM in (b) in a single-scene image collected on 29 January 2022. The results reveal the distinct deviations from the nominal centre wavelength and FWHM among different track pixels during satellite imaging. **Figure 8(c)** displays the ΔXCH_4 of the corrected image, capturing plumes seen in **Figures 3(b), 6(c),** and **6(d)**, among others. **Figures 8(d)** and **8(e)** show the evident striping differences and spectral calibration's impact on calculating ΔXCH_4 of individual plume. The difference can reach up to 100 ppb. To further assess the spectral calibration's influence on CH_4 point source estimation, this study analysed the shift in centre wavelength and changes in FWHM in 111 representative scenes with potential point source emissions using GF-5B/AHSI, as shown in **Figures 9(a)** and **9(b)**. The results indicate that the average shift in centre wavelength of GF-5B/AHSI is approximately -0.05 nm, mostly ranging between -0.2 and 0.1 nm. The ratio of change in FWHM averages around 1.1, predominantly falling between 1.0 and 1.25 times (between 0-2.13 nm). Furthermore, the study evaluated the impact of spectral shift and FWHM change on the estimation of point source emission flux rate, as shown in **Figures 9(c) and 9(d)**. The results indicate that the caused difference of point source emission flux rate ranges from 0.49 to 564.20 $kg \cdot h^{-1}$. The average percentage of change is $(1.78\pm1.39)\%$. The maximum difference reaches up to about 5.0%. By considering the shift in central wavelength and change in FWHM in the spectral observations, it exhibits a potential to reduce the uncertainty of XCH_4 emission rate estimation using GF-5B/AHSI.

(2) Impact of heterogeneous surface features

Complex surface features significantly affect the identification of suspected point sources based on ΔXCH_4 maps and the derivation of point source emissions. In this study, we originally observed 219 instances of 113 suspicious point sources. In a more refined identification of these sources, we cross-checked and confirmed their positions using ΔXCH_4 retrievals from GF-5B/AHSI against high-resolution Google Earth imagery. Our findings revealed that the identification of point sources was significantly affected by the complex surfaces that exhibit strong SWIR absorption similar to CH_4 and therefore result in false positive signal. Notably, array of solar panels that are widespread in Shanxi is the primary disruptor of the spectral matched filter retrieval method. An example of solar panel arrays is shown in **Figure 10**. Moreover, we found that surface features such as greenhouse structures, certain buildings, water bodies with plume-like distributions, and moist cultivated lands (like paddy fields) also generated noticeable high-value ΔXCH_4 interference signals. Therefore, in CH_4 point source detection using GF-5B image, it's essential to consider combine with high resolution images to filter out false positive signals.

(3) Evaluating wind fields from ERA5 reanalysis using observations from meteorological stations in Shanxi

Wind fields, including wind speed and direction, are the primary drivers of uncertainty in estimating point source emissions, especially in plume segmentation and flux rate calculations. For plume segmentation, instead of visual interpretation, this study introduces the flood-fill method. Accurate wind direction information enables us to precisely narrow down the flood-fill search directions, thereby removing abnormal signals from non-point source emissions, enhancing the reliability of plume segmentation. In emission flux rate estimation, aligning with previous studies, this study defined an uncertainty in ERA5 wind speed as 50%, thus leading to a significant uncertainty in the estimated emission rate. To evaluate the uncertainty of the wind fields from ERA5 reanalysis, which is widely used in many previous studies, this study compared them with data from three ground-based meteorological sites in Shanxi over the concentrated point source areas (**Figure 11**). The comparison results indicate that from 2021 to 2023, the overall bias in the ERA5 wind speed was approximately 1.30 m/s, which is close to 100% of bias on average. It has been recognized that the wind speed should be in a moderate range to allow detectable plumes from space. Too small wind speed may hamper the plume to develop, while too large wind speed may dilute the plume. It is observed in our cases that the wind speeds roughly fall within 0.5 to 2.5 $m \cdot s^{-1}$ for most days with detectable point source plumes. If we assume this is the suitable wind speed range for satellite detection, as shown in black dots in the upper panel of **Figure 11**, the deviation is about 0.45-0.54 $m \cdot s^{-1}$, which is close to about 50% of the wind speed from ERA5. This uncertainty is consistent with the assumption of wind speed uncertainty (50%) in this study. In terms of wind direction, there are significant differences between ERA5 and the observations from meteorological sites. While ERA5 reanalysis data (at a height of 10-meter) show relatively constant wind direction, the measurements of wind direction from meteorological stations show a much larger range. This discrepancy indicates significant deviations between ERA5 reanalysis wind fields and actual wind conditions, challenging their direct application in point source plume identification and emission estimation. Consequently, leveraging high-density and high-precision meteorological observations from automatic meteorological monitoring stations, especially over regions with complex surface properties, could reduce the uncertainty and enhance the accuracy of satellite-based detection and estimation of CH_4 point source emissions.

https://doi.org/10.5194/egusphere-2023-3047
Preprint. Discussion started: 20 December 2023

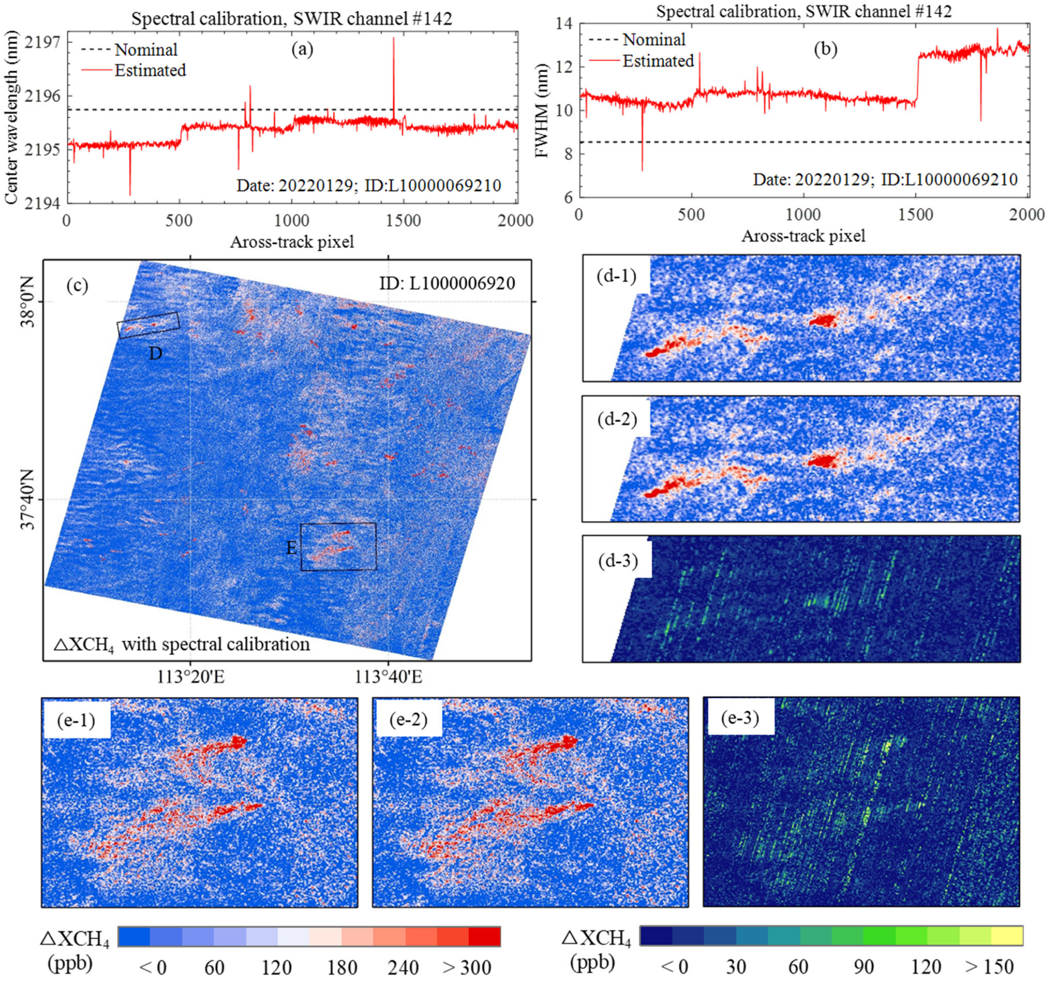

385 **Figure 8. Example of the shift in centre wavelength and FWHM change for across-track pixels of channel #142 from GF-5B/AHSI SWIR imagery and their impacts for ΔXCH₄ retrieval. (a) shows the shift in centre wavelength for across-track pixels; (b) shows the FWHM variation ratio for across-track pixels; (c) shows the ΔXCH₄ retrieval of a single image with inputs of updated spectral calibration parameters; (d) and (e) are the comparison of zoom in plumes with and without inputs of updated spectral calibration parameters, in which (d-1) and (e-1) are results without calibration, and (d-2) and (e-2) are results with calibration, and (d-3) and**
390 **(e-3) are the corresponding difference in ΔXCH₄ retrieval.**

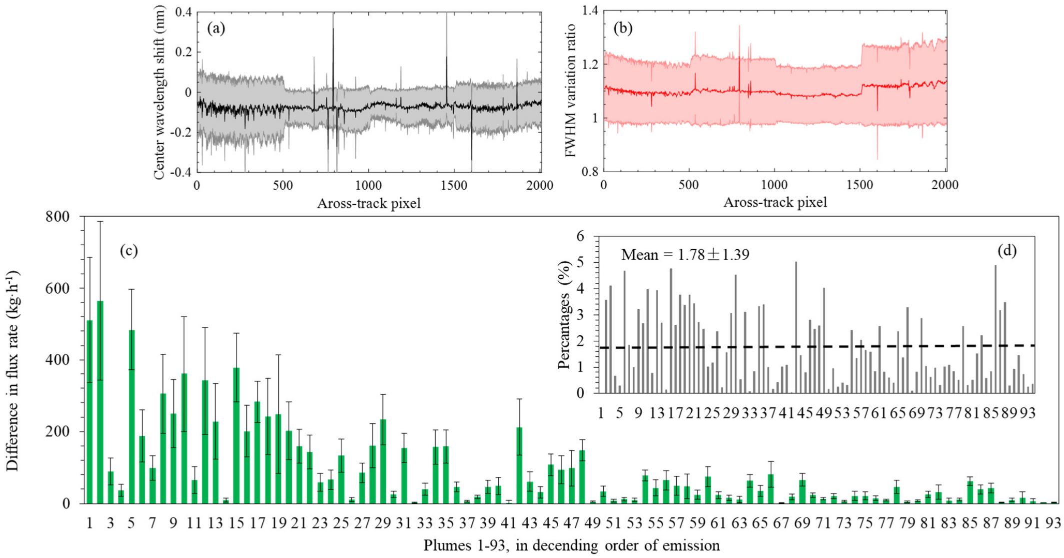

Figure 9. Statistics of the shift in centre wavelength in (a) and FWHM variation ratio in (b) of all 111 GF-5B/AHSI SWIR images with potential CH_4 point sources. The difference in the estimations of emission flux rates in (c) and corresponding difference in percentages in (d) for all detected CH_4 plumes shown in Figure 6 and Figure 7.

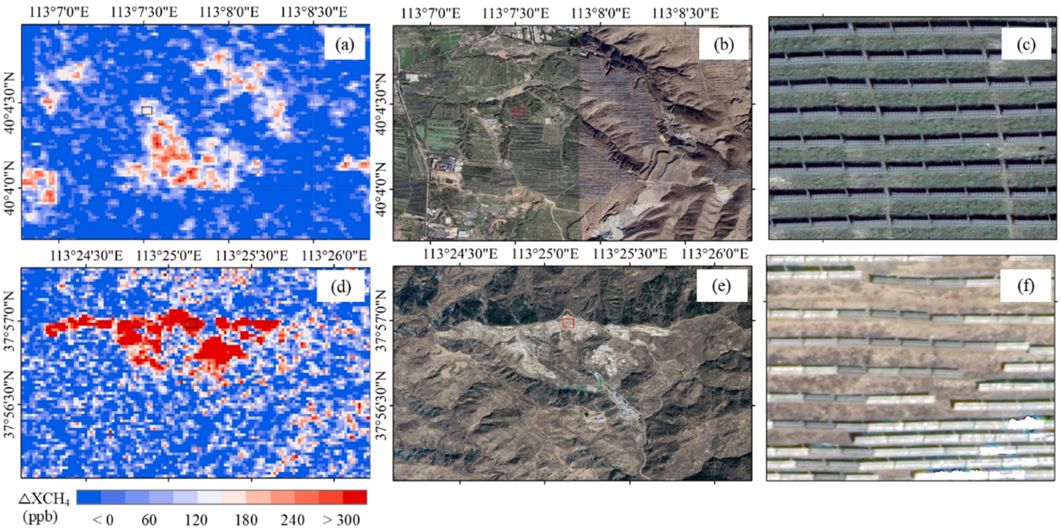

Figure 10. Examples of the impact of array of solar panels, which generates false positive signals, on the ΔXCH_4 retrieval in Shanxi. ΔXCH_4 retrievals with high values are similar to plume shapes in (a) and (d). There false positive signals are caused by the similar patterns of solar panel arrays, which can be seen from high resolution of © Google Maps in (b) and (e). Zoom in details of solar panels in the red boxes in (b) and (e) can be found in (c) and (f), respectively.

https://doi.org/10.5194/egusphere-2023-3047
Preprint. Discussion started: 20 December 2023

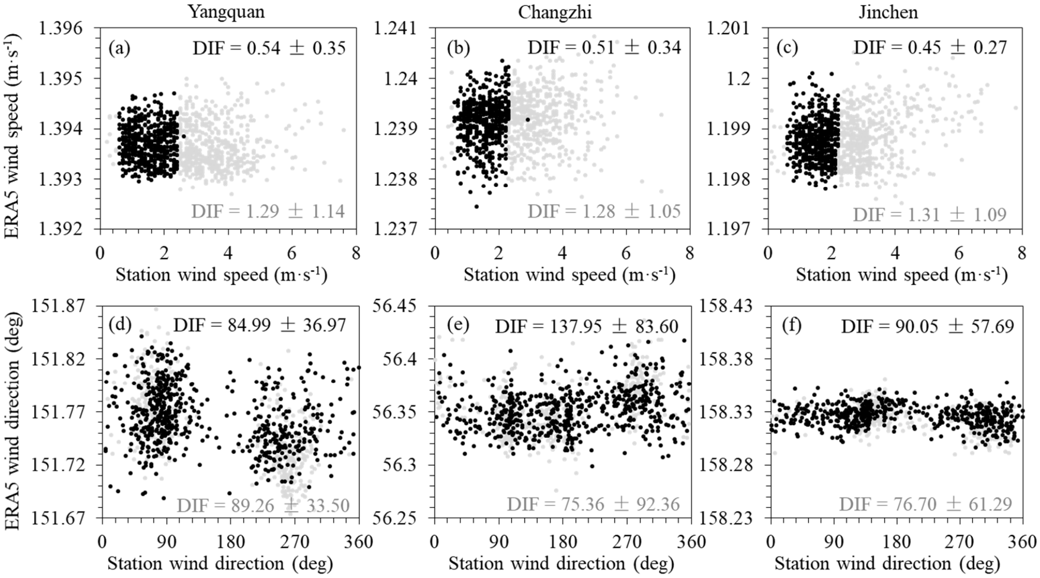

405 **Figure 11. Comparison of wind speeds (a-c) and directions (d-f) between ERA5 reanalysis and meteorological stations located in Yangquan, Changzhi and Jincheng cities in Shanxi, as indicated in Figure 1. Wind fields data from 2021 to 2023 are extracted in the daytime correspond to the GF-5B overpass time. Black dot data are selected according to the wind speed range of 0.5 to 2.5 m·s^{-1}.**

https://doi.org/10.5194/egusphere-2023-3047
Preprint. Discussion started: 20 December 2023

5. Summary

In this study, we conducted a survey of CH_4 point sources emissions from coal mines in Shanxi, China using hyperspectral observations of GF-5B/AHSI. We first carried out the spectral calibration based on the estimates of the across-track changes in channel center wavelength and FWHM, which are approximately -0.05 nm and 10%, respectively. We adopted the widely used matched filter method to calculate the enhancement ΔXCH_4. Based on the enhancement, the emission plumes are extracted using the fill-flood method, which is an automated plume segmentation method. The emission flux rate and the associated uncertainty are eventually estimated using IME method. Our results show that the errors caused by spectral calibration (wavelength shift and FWHM change) and the selection of different background can reach up to 5.0% and 8.5%, respectively. Simultaneously, this study presents the spatial distribution and emission flux rates of 32 point sources and 93 observed plumes in Shanxi province from 2021 to 2023. The findings indicate that coal mine sources in Shanxi are primarily located around Yangquan, Changzhi, and Jincheng areas, with plume emission flux rates ranging from 857.67 ± 207.34 (the minimum) to 14333.02 ± 5249.32 $kg \cdot h^{-1}$ (the maximum). Multiple repeated observations show significant differences in emission flux rates from the same source. The difference can reach to 11497.79 $kg \cdot h^{-1}$ with a different by a factor of more than 7 times between the maximum and the minimum, indicating that a single overpass observation cannot represent the overall emissions of the point source. Assuming median values from multiple observations represent point source emission rates, simultaneous emission flux rates from all sources in Shanxi would reach 13.26 $t \cdot h^{-1}$. This study highlights that wind speed remains the primary factor contributing to uncertainty in point source emission estimation (approximately 84.84%), yet the uncertainty of IME (approximately 15.16%) is also important.

It is important to note that the plume shapes detected based solely on the ΔXCH_4 maps contains false positive signals due to surface interference. The strong absorption in SWIR by certain surface types significantly disrupts point source detection and flux rate emissions. In the future, a fusion of hyperspectral spectra and multispectral image with high spatial resolution could effectively filter out false positive signals and remove surface covering interference. In addition, the uncertainty of wind field data remains significant sources of uncertainty in CH_4 point source emission flux rate estimation. From the evaluation of the accuracy of wind fields in ECMWF ERA5 reanalysis by comparing with ground-based meteorological station, we found large discrepancy, especially in wind directions. For regions with complex terrain like Shanxi, incorporating local meteorological measurements into the detection of CH_4 point source are important to achieve high accuracy.

Data availability:

Gaofen-5B AHSI images are downloaded from China Centre for Resources Satellite Data and Application, accessed from https://data.cresda.cn/#/home. Official applications are required for accessing the GF-5B/AHSI spectra. ERA5 reanalysis data from ECMWF can be accessed from https://cds.climate.copernicus.eu/cdsapp#!/home. Observations from national weather stations data are from China Meteorological Administration Data Centre, accessed from http://data.cma.cn/en. The dataset of detected plumes in Shanxi province of China during 2021-2023 using Gaofen-5B AHSI data will be made available upon publication.

Author contributions:

ZZ designed the study. ZH prepared all datasets, carried out the retrieval and result analysis. ZZ developed the retrieval codes. ZH wrote the first draft of the manuscript. LG and ML contributed to data acquisition and results analysis. All authors reviewed and proofread the manuscript.

Acknowledgement:

We thank Drs. L. Guanter, Y. Liu, and C. Sun for helpful discussions at the early stage of this work. This study was funded by the National Natural Science Foundation of Zhejiang Province (Nos. LQ21d050001) and the Research and development Project of “Jianbing” “Lingyan” of Zhejiang Province (NO. 2023C03190). Z.-C. Zeng acknowledges funding from the National Natural Science Foundation of China (grant no. 42275142 and no. 12292981). This work was also supported by High-performance Computing Platform of Peking University. We thank the support from the China Meteorological Administration Youth Innovation Team (Development and application of key technologies for greenhouse gas observation).

Competing interests.

The contact author has declared that none of the authors has any competing interests.

References

Chen, D., Chen, A., Hu, X., Li, B., Li, X., Guo, L., Feng, R., Yang, Y., and Fang, X.: Substantial methane emissions from abandoned coal mines in China, Environmental Research, 214, 113944, 2022a.

Chen, Z., Jacob, D. J., Nesser, H., Sulprizio, M. P., Lorente, A., Varon, D. J., Lu, X., Shen, L., Qu, Z., Penn, E., and Yu, X.: Methane emissions from China: a high-resolution inversion of TROPOMI satellite observations, Atmospheric Chemistry and Physics, 22, 10809-10826, 10.5194/acp-22-10809-2022, 2022b.

Chen, Z., Jacob, D. J., Gautam, R., Omara, M., Stavins, R. N., Stowe, R. C., Nesser, H., Sulprizio, M. P., Lorente, A., Varon, D. J., Lu, X., Shen, L., Qu, Z., Pendergrass, D. C., and Hancock, S.: Satellite quantification of methane emissions and oil–gas methane intensities from individual countries in the Middle East and North Africa: implications for climate action, Atmospheric Chemistry and Physics, 23, 5945-5967, 10.5194/acp-23-5945-2023, 2023.

Cusworth, D. H., Duren, R. M., Thorpe, A. K., Tseng, E., Thompson, D., Guha, A., Newman, S., Foster, K. T., and Miller, C. E.: Using remote sensing to detect, validate, and quantify methane emissions from California solid waste operations, Environmental Research Letters, 15, 054012, 10.1088/1748-9326/ab7b99, 2020.

Duren, R. M., Thorpe, A. K., Foster, K. T., Rafiq, T., Hopkins, F. M., Yadav, V., Bue, B. D., Thompson, D. R., Conley, S., Colombi, N. K., Frankenberg, C., McCubbin, I. B., Eastwood, M. L., Falk, M., Herner, J. D., Croes, B. E., Green, R. O., and Miller, C. E.: California's methane super-emitters, Nature, 575, 180-184, 10.1038/s41586-019-1720-3, 2019.

Ehret, T., De Truchis, A., Mazzolini, M., Morel, J.-M., D'aspremont, A., Lauvaux, T., Duren, R., Cusworth, D., and Facciolo, G.: Global tracking and quantification of oil and gas methane emissions from recurrent sentinel-2 imagery, Environmental science & technology, 56, 10517-10529, 2022.

Farr, T. G., Rosen, P. A., Caro, E., Crippen, R., Duren, R., Hensley, S., Kobrick, M., Paller, M., Rodriguez, E., Roth, L., Seal, D., Shaffer, S., Shimada, J., Umland, J., Werner, M., Oskin, M., Burbank, D., and Alsdorf, D.: The Shuttle Radar Topography Mission, Reviews of Geophysics, 45, 10.1029/2005rg000183, 2007.

Frankenberg, C., Thorpe, A. K., Thompson, D. R., Hulley, G., Kort, E. A., Vance, N., Borchardt, J., Krings, T., Gerilowski, K., Sweeney, C., Conley, S., Bue, B. D., Aubrey, A. D., Hook, S., and Green, R. O.: Airborne methane remote measurements reveal heavy-tail flux distribution in Four Corners region, Proceedings of the National Academy of Sciences, 113, 9734-9739, doi:10.1073/pnas.1605617113, 2016.

Guanter, L., Segl, K., Sang, B., Alonso, L., Kaufmann, H., and Moreno, J.: Scene-based spectral calibration assessment of high spectral resolution imaging spectrometers, Opt. Express, 17, 11594-11606, 10.1364/OE.17.011594, 2009.

Guanter, L., Irakulis-Loitxate, I., Gorroño, J., Sánchez-García, E., Cusworth, D. H., Varon, D. J., Cogliati, S., and Colombo, R.: Mapping methane point emissions with the PRISMA spaceborne imaging spectrometer, Remote Sensing of Environment, 265, 112671, 10.1016/j.rse.2021.112671, 2021.

Guanter, L., Kaufmann, H., Segl, K., Foerster, S., Rogass, C., Chabrillat, S., Kuester, T., Hollstein, A., Rossner, G., Chlebek, C., Straif, C., Fischer, S., Schrader, S., Storch, T., Heiden, U., Mueller, A., Bachmann, M., Mühle, H., Müller, R., Habermeyer, M., Ohndorf, A., Hill, J., Buddenbaum, H., Hostert, P., Van der Linden, S., Leitão, P. J., Rabe, A., Doerffer, R., Krasemann, H., Xi, H., Mauser, W., Hank, T., Locherer, M., Rast, M., Staenz, K., and Sang, B.: The EnMAP Spaceborne Imaging Spectroscopy Mission for Earth Observation, Remote Sensing, 7, 8830-8857, 2015.

He, Z., Lei, L., Welp, L., Zeng, Z.-C., Bie, N., Yang, S., and Liu, L.: Detection of Spatiotemporal Extreme Changes in Atmospheric CO_2 Concentration Based on Satellite Observations, Remote Sensing, 10, 839, 10.3390/rs10060839, 2018.

Huang, Y., Natraj, V., Zeng, Z. C., Kopparla, P., and Yung, Y. L.: Quantifying the impact of aerosol scattering on the retrieval of methane from airborne remote sensing measurements, Atmos. Meas. Tech., 13, 6755-6769, 10.5194/amt-13-6755-2020, 2020.

IPCC: Climate Change 2021: The Physical Science Basis, Contribution of Working Group I to the Sixth Assessment Report of the Intergovernmental Panel on Climate Change, Cambridge University Press, Cambridge, UK and New York, NY, USA, 10.1017/9781009157896, 2021.

Irakulis-Loitxate, I., Guanter, L., Liu, Y.-N., Varon, D. J., Maasakkers, J. D., Zhang, Y., Chulakadabba, A., Wofsy, S. C., Thorpe, A. K., and Duren, R. M.: Satellite-based survey of extreme methane emissions in the Permian basin, Science advances, 7, eabf4507, 2021.

Jacob, D. J., Varon, D. J., Cusworth, D. H., Dennison, P. E., Frankenberg, C., Gautam, R., Guanter, L., Kelley, J., McKeever, J., Ott, L. E., Poulter, B., Qu, Z., Thorpe, A. K., Worden, J. R., and Duren, R. M.: Quantifying methane emissions from the global scale down to point sources using satellite observations of atmospheric methane, Atmospheric Chemistry and Physics, 22, 9617-9646, 10.5194/acp-22-9617-2022, 2022.

Jervis, D., McKeever, J., Durak, B. O. A., Sloan, J. J., Gains, D., Varon, D. J., Ramier, A., Strupler, M., and Tarrant, E.: The GHGSat-D imaging spectrometer, Atmospheric Measurement Techniques, 14, 2127-2140, 10.5194/amt-14-2127-2021, 2021.

Jongaramrungruang, S., Matheou, G., Thorpe, A. K., Zeng, Z. C., and Frankenberg, C.: Remote sensing of methane plumes: instrument tradeoff analysis for detecting and quantifying local sources at global scale, Atmos. Meas. Tech., 14, 7999-8017, 10.5194/amt-14-7999-2021, 2021.

Lauvaux, T., Giron, C., Mazzolini, M., d'Aspremont, A., Duren, R., Cusworth, D., Shindell, D., and Ciais, P.: Global assessment of oil and gas methane ultra-emitters, Science, 375, 557-561, 2022.

Li, F., Sun, S., Zhang, Y., Feng, C., Chen, C., Mao, H., and Liu, Y.: Mapping methane super-emitters in China and United States with GF5-02 hyperspectral imaging spectrometer, National Remote Sensing Bulletin, 0, 1-15, 10.11834/jrs.20232453, 2023.

Liu, Q., Yu, T., and Zhang, W.: Validation of GaoFen-1 Satellite Geometric Products Based on Reference Data, Journal of the Indian Society of Remote Sensing, 47, 1331-1346, 10.1007/s12524-019-01017-2, 2019a.

Liu, Y.-N., Sun, D.-X., Hu, X.-N., Ye, X., Li, Y.-D., Liu, S.-F., Cao, K.-Q., Chai, M.-Y., Zhang, J., and Zhang, Y.: The advanced hyperspectral imager: aboard China's GaoFen-5 satellite, IEEE Geoscience and Remote Sensing Magazine, 7, 23-32, 2019b.

Lu, X., Jacob, D. J., Wang, H., Maasakkers, J. D., Zhang, Y., Scarpelli, T. R., Shen, L., Qu, Z., Sulprizio, M. P., Nesser, H., Bloom, A. A., Ma, S., Worden, J. R., Fan, S., Parker, R. J., Boesch, H., Gautam, R., Gordon, D., Moran, M. D., Reuland, F., Villasana, C. A. O., and Andrews, A.: Methane emissions in the United States, Canada, and Mexico: evaluation of national methane emission inventories and 2010–2017 sectoral trends by inverse analysis of in situ (GLOBALVIEWplus CH_4 ObsPack) and satellite (GOSAT) atmospheric observations, Atmospheric Chemistry and Physics, 22, 395-418, 10.5194/acp-22-395-2022, 2022.

Miller, S. M., Michalak, A. M., Detmers, R. G., Hasekamp, O. P., Bruhwiler, L. M. P., and Schwietzke, S.: China's coal mine methane regulations have not curbed growing emissions, Nature communications, 10, 10.1038/s41467-018-07891-7, 2019.

Muñoz-Sabater, J., Dutra, E., Agustí-Panareda, A., Albergel, C., Arduini, G., Balsamo, G., Boussetta, S., Choulga, M., Harrigan, S., and Hersbach, H.: ERA5-Land: A state-of-the-art global reanalysis dataset for land applications, Earth system science data, 13, 4349-4383, 2021.

Pandey, S., Houweling, S., Lorente, A., Borsdorff, T., Tsivlidou, M., Bloom, A. A., Poulter, B., Zhang, Z., and Aben, I.: Using satellite data to identify the methane emission controls of South Sudan's wetlands, Biogeosciences, 18, 557-572, 10.5194/bg-18-557-2021, 2021.

Qin, K., Hu, W., He, Q., Lu, F., and Cohen, J. B.: Individual Coal Mine Methane Emissions Constrained by Eddy-Covariance Measurements: Low Bias and Missing Sources, EGUsphere, 2023, 1-49, 10.5194/egusphere-2023-1210, 2023.

Sánchez-García, E., Gorroño, J., Irakulis-Loitxate, I., Varon, D. J., and Guanter, L.: Mapping methane plumes at very high spatial resolution with the WorldView-3 satellite, Atmospheric Measurement Techniques, 15, 1657-1674, 10.5194/amt-15-1657-2022, 2022.

Saunois, M., Stavert, A. R., Poulter, B., Bousquet, P., Canadell, J. G., Jackson, R. B., Raymond, P. A., Dlugokencky, E. J., Houweling, S., Patra, P. K., Ciais, P., Arora, V. K., Bastviken, D., Bergamaschi, P., Blake, D. R., Brailsford, G., Bruhwiler, L., Carlson, K. M., Carrol, M., Castaldi, S., Chandra, N., Crevoisier, C., Crill, P. M., Covey, K., Curry, C. L., Etiope, G., Frankenberg, C., Gedney, N., Hegglin, M. I., Höglund-Isaksson, L., Hugelius, G., Ishizawa, M., Ito, A., Janssens-Maenhout,

https://doi.org/10.5194/egusphere-2023-3047
Preprint. Discussion started: 20 December 2023

G., Jensen, K. M., Joos, F., Kleinen, T., Krummel, P. B., Langenfelds, R. L., Laruelle, G. G., Liu, L., Machida, T., Maksyutov, S., McDonald, K. C., McNorton, J., Miller, P. A., Melton, J. R., Morino, I., Müller, J., Murguia-Flores, F., Naik, V., Niwa, Y., Noce, S., O'Doherty, S., Parker, R. J., Peng, C., Peng, S., Peters, G. P., Prigent, C., Prinn, R., Ramonet, M., Regnier, P., Riley, W. J., Rosentreter, J. A., Segers, A., Simpson, I. J., Shi, H., Smith, S. J., Steele, L. P., Thornton, B. F., Tian, H., Tohjima, Y., Tubiello, F. N., Tsuruta, A., Viovy, N., Voulgarakis, A., Weber, T. S., van Weele, M., van der Werf, G. R., Weiss, R. F., Worthy, D., Wunch, D., Yin, Y., Yoshida, Y., Zhang, W., Zhang, Z., Zhao, Y., Zheng, B., Zhu, Q., Zhu, Q., and Zhuang, Q.: The Global Methane Budget 2000–2017, Earth System Science Data, 12, 1561-1623, 10.5194/essd-12-1561-2020, 2020.

Schuit, B. J., Maasakkers, J. D., Bijl, P., Mahapatra, G., van den Berg, A.-W., Pandey, S., Lorente, A., Borsdorff, T., Houweling, S., Varon, D. J., McKeever, J., Jervis, D., Girard, M., Irakulis-Loitxate, I., Gorroño, J., Guanter, L., Cusworth, D. H., and Aben, I.: Automated detection and monitoring of methane super-emitters using satellite data, Atmospheric Chemistry and Physics, 23, 9071-9098, 10.5194/acp-23-9071-2023, 2023.

Thompson, D. R., Thorpe, A. K., Frankenberg, C., Green, R. O., Duren, R., Guanter, L., Hollstein, A., Middleton, E., Ong, L., and Ungar, S.: Space-based remote imaging spectroscopy of the Aliso Canyon CH4 superemitter, Geophysical Research Letters, 43, 6571-6578, 10.1002/2016gl069079, 2016.

Thorpe, A. K., Green, R. O., Thompson, D. R., Brodrick, P. G., Chapman, J. W., Elder, C. D., Irakulis-Loitxate, I., Cusworth, D. H., Ayasse, A. K., Duren, R. M., Frankenberg, C., Guanter, L., Worden, J. R., Dennison, P. E., Roberts, D. A., Chadwick, K. D., Eastwood, M. L., Fahlen, J. E., and Miller, C. E.: Attribution of individual methane and carbon dioxide emission sources using EMIT observations from space, Science advances, 9, eadh2391, doi:10.1126/sciadv.adh2391, 2023.

Varon, D. J., Jervis, D., McKeever, J., Spence, I., Gains, D., and Jacob, D. J.: High-frequency monitoring of anomalous methane point sources with multispectral Sentinel-2 satellite observations, Atmospheric Measurement Techniques, 14, 2771-2785, 10.5194/amt-14-2771-2021, 2021.

Varon, D. J., Jacob, D. J., McKeever, J., Jervis, D., Durak, B. O. A., Xia, Y., and Huang, Y.: Quantifying methane point sources from fine-scale satellite observations of atmospheric methane plumes, Atmospheric Measurement Techniques, 11, 5673-5686, 10.5194/amt-11-5673-2018, 2018.

Varon, D. J., McKeever, J., Jervis, D., Maasakkers, J. D., Pandey, S., Houweling, S., Aben, I., Scarpelli, T., and Jacob, D. J.: Satellite Discovery of Anomalously Large Methane Point Sources From Oil/Gas Production, Geophysical Research Letters, 46, 13507-13516, 10.1029/2019gl083798, 2019.

Zeng, Z., Natraj, V., Xu, F., Chen, S., Gong, F.-Y., Pongetti, T. J., Sung, K., Toon, G. C., Sander, S. P., and Yung, Y. L.: GFIT3: A full physics retrieval algorithm for remote sensing of greenhouse gases in the presence of aerosols, Atmospheric Measurement Techniques, 2021.

Zheng, C., Jiang, B., Xue, S., Chen, Z., and Li, H.: Coalbed methane emissions and drainage methods in underground mining for mining safety and environmental benefits: A review, Process Safety and Environmental Protection, 127, 103-124, https://doi.org/10.1016/j.psep.2019.05.010, 2019.

Zscheischler, J., Mahecha, M. D., Harmeling, S., and Reichstein, M.: Detection and attribution of large spatiotemporal extreme events in Earth observation data, Ecological Informatics, 15, 66-73, 10.1016/j.ecoinf.2013.03.004, 2013.

Appendix A: Geometric localization of GF-5B/AHSI images

The identification of CH_4 point sources using high-resolution satellite imagery is closely linked to land cover, while the accurate calculation of ΔXCH_4 is significantly affected by spectral differences in the background within the study area. Hence, precise geometric localization (Equations 4–6) of the GF-5B satellite images is crucial. The retrieval of ΔXCH_4 involves both forward and inverse computations of the Rational Polynomial Coefficients (RPCs) in high-resolution imagery (**Liu et al., 2019**). The forward computation entails transforming the row and column indices (Row_i, Col_i) of the image data into geographical coordinates (Lat_i, Lon_i), aiding in detecting and identifying ΔXCH_4 point sources. Conversely, the reverse computation aims to optimize background concentration calculations by transforming detected point source geographical coordinates back to the image's row and column indices.

$$\begin{cases} Row_i = F_a(U_i, V_i, W)/F_b(U_i, V_i, W_i) \\ Col_i = F_c(U_i, V_i, W)/F_d(U_i, V_i, W_i) \end{cases} \tag{4}$$

$$F_a(\mathrm{U}, \mathrm{V}, \mathrm{W}) = a_1 + a_2V + a_3U + a_4W + a_5VU + a_6VW + a_7UW + a_8V^2 + a_9U^2 + a_{10}W^2 + a_{11}UVW + a_{12}V^3 + a_{13}VU^2 + a_{14}VW^2 + a_{15}V^2U + a_{16}V^3 + a_{17}UW^2 + a_{18}V^2W + a_{19}\mathrm{U}^2\mathrm{W} + a_{20}\mathrm{W}^3 \tag{5}$$

$$\begin{cases} U_i = (Lat_i - Lat\_off)/Lat\_scale \\ V_i = (Lon_i - Lon\_off)/Lon\_scale \\ W_i = (Height_i - Heigh\_off)/Heigh\_scale \end{cases} \tag{6}$$

where，$a_1 \dots a_{20}$，$b_1 \dots b_{20}$, $c_1 \dots c_{20}$, $d_1 \dots d_{20}$, Lat_off, Lat_scale, Lon_off, Lon_scale, $Heigh\_off$ and $Heigh\_scale$ are rational polynomial coefficients (RPCs), which can be obtained from incidental data of the GF-5B images.